Xueke Zheng
UM-SJTU Joint Institute,
Shanghai Jiao Tong University,
Shanghai 200240, China
e-mail: zxk2046@sjtu.edu.cn

Cheng Zhuang
UM-SJTU Joint Institute,
Shanghai Jiao Tong University,
Shanghai 200240, China
e-mail: Mike.Z.C@sjtu.edu.cn

Shuixin Xiao
UM-SJTU Joint Institute,
Shanghai Jiao Tong University,
Shanghai 200240, China
e-mail: xiaoshuixin@sjtu.edu.cn

Yu Qiu
SAIC Motor Corporation Limited,
Shanghai 201800, China
e-mail: qiuyu_1123@163.com

Jun Zhang
UM-SJTU Joint Institute,
Department of Automation,
Shanghai Jiao Tong University,
Shanghai 200240, China
e-mail: zhangjun12@sjtu.edu.cn

Mian Li[1]
Professor
Fellow ASME
UM-SJTU Joint Institute,
Global Institute of Future Technology,
Department of Automation,
Shanghai Jiao Tong University,
Shanghai 200240, China
e-mail: mianli@sjtu.edu.cn

Signal Estimation for Vehicle Body Accelerations Using Piecewise Linear System Identification in the Frequency Domain

In this work, we investigate a signal estimation problem which is common and critical for durability design of vehicle bodies. The relation between the frequency responses of accelerometers is the target to model so that the ones of easy-to-measure accelerometers can estimate the responses of hard-to-measure accelerometers. A piecewise linear frequency-domain identification method relying on finite impulse response (FIR) models is proposed and performed to tackle the nonlinearity issue in the signal estimation problems: first, the interesting frequency range is segmented into three subranges which are clearly identified by peak histograms of frequency signals. Then, FIR models which provide a satisfactory description of the system are constructed to estimate the frequency responses of the interesting signals at subranges, one for each. The performance of the proposed approach is validated by using real-world data under multiple working conditions. The results show that the proposed method has a good estimation accuracy, and it brings the benefit that the number of accelerometers can be significantly reduced during the durability design of vehicle bodies. [DOI: 10.1115/1.4054306]

Keywords: data-driven engineering, model-based systems engineering, process modeling for engineering applications, qualification, verification and validation of computational models

1 Introduction

When designing a new vehicle, original equipment manufacturers (OEMs) perform direct measurements of vehicle body accelerations during so-called road load data acquisition (RLDA) testing campaigns during which prototype vehicles are driven on proving grounds or public roads [1–3]. The data of vehicle body accelerations collected from RLDA testing campaigns contain durability information which is valuable in the laboratory for the shaker test. With the data of vehicle body accelerations and the shaker test, the durability design of the vehicle body can be verified if the vehicle body under test is capable of withstanding the anticipated environmental vibration throughout its service life [4].

During RLDA testing campaigns, multiple prototype vehicles are needed to acquire data from a range of different road types [2]. However, two critical issues make the RLDA testing campaigns quite restrictive:

(i) The cost of these high-performance accelerometers can be very high, and thus the automobile manufacturers may not be able or willing to equip multiple prototype vehicles with these accelerometers.
(ii) Deployment, maintenance, and repairing of accelerometers could take much time and effort.

Soft sensors which are inferential models that use easy-to-measure variables to estimate hard-to-measure variables have been reported to deliver similar information as their hardware counterparts [5–7]. Note that the data of hard-to-measure variables are usually not available in most times (e.g., the online estimation process) other than a short of time (e.g., the offline training process). Two classes of soft sensors, namely, model-driven (most commonly based on first-principle models) and data-driven (based on black-box models developed from the data), are distinguished at a very general level. Due to the complex structures of vehicles [8–10], highly accurate first-principle models are usually difficult to obtain or are not available for practical applications [11].

Black-box system identification approaches have proven to be effective in control design [12,13], prediction [14,15], simulation [16,17], and diagnosis/fault detection of dynamic systems [18,19] and have witnessed great success in these areas. To overcome the vibration estimation issue for prototype vehicles, this work aims to develop black-box models to connect different signals collected from accelerometers such that some of them can be estimated by others. As shown in Fig 1, the overall proposed procedure can be divided into two stages:

(i) During the offline stage, one of the prototype vehicles is equipped with all accelerometers to construct black-box models from the responses of easy-to-measure accelerations to the responses of hard-to-measure accelerations.

[1]Corresponding author.
Manuscript received December 22, 2021; final manuscript received April 6, 2022; published online May 17, 2022. Assoc. Editor: Bin He.

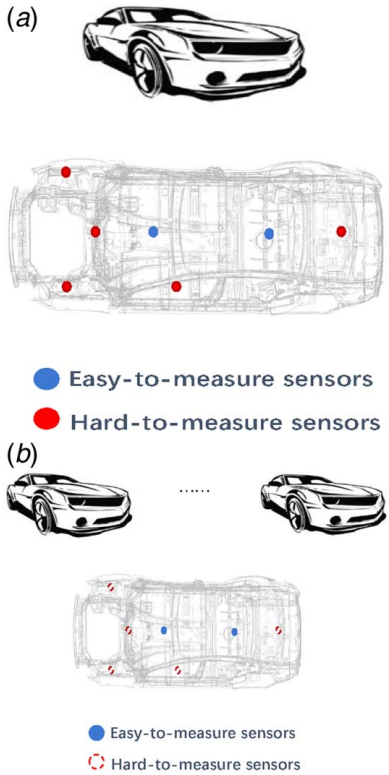

Fig. 1 The procedure at the (*a*) offline and (*b*) online stages

(ii) During the online stage, only easy-to-measure accelerometers are deployed on each prototype vehicle. The signals collected from these easy-to-measure accelerometers at each prototype vehicle are fed into the corresponding black-box models to estimate the hard-to-measure signals.

The problem during the offline stage can be regarded as sensor-to-sensor system identification problems which are less typical ones in the system identification community [20–24]. In sensor-to-sensor problems, the true inputs of systems are unknown. For example, the excitation from the road is unknown when vehicles are driven under random working conditions. Transmissibilities are introduced to model the relation between the signals collected from different sensors if the true systems can be approximated by linear time invariant (LTI) systems [21–24]. Moreover, transmissibilities can be approximated by finite impulse response (FIR) models that have been widely used in recent years [25–28], given the following reasons [24,29,30]:

(i) FIR models are bounded-inputs bounded-output stable [31].
(ii) The computational cost and memory requirements for hardware implementations of FIR models are low.
(iii) The process of model tuning is time-effective, and the size of data sets required for identifying FIR parameters is usually small, compared to other data-driven models, due to their simple structures.

Fig. 2 The locations of vehicle body accelerometers

However, when it comes to estimate the responses at interesting locations of vehicle bodies, the behaviors of vehicle systems are nonlinear due to the complex structures of suspensions, tires, and other components (the existence of the nonlinearity is also verified in Sec. 4.3 in this work). For instance, the spring and damping forces of suspension systems are nonlinear with respect to the deformation of the spring, the relative velocity between the extremes of the damper, the excitation amplitude, or the excitation frequency [9,11].

On the other hand, the decisions on using the time or frequency-domain system identification approaches may depend on choices on the specific applications from a practical point of view. For certain engineering applications, frequency-domain approaches can make prefiltering, condensing large data sets, and combining experiments easily implemented [32]. For example, when dealing with systems having a fairly wide spread of time constants, large data sets have to be collected in the time domain, while they can be condensed easily by only considering a subset of the entire frequency range.

This work aims to construct high-accuracy black-box models from the easy-to-measure accelerations to the hard-to-measure accelerations such that easy-to-measure accelerations can estimate the hard-to-measure accelerations in the frequency domain. A piecewise linear system identification approach in the frequency domain is proposed in order to overcome the nonlinearity issue: the interesting frequency range is segmented into three subranges in terms of peak histograms of all accelerations with three steps: determining the noise level, selecting peaks, and segmenting the interesting frequency range. Then noncausal FIR models which provide a satisfactory description of the system at subranges are developed, one for each. The proposed method is successfully validated in the sense that the estimation accuracy is almost 90% for 14 hard-to-measure accelerations under 70 working conditions by using only two easy-to-measure accelerometers. To the authors' best knowledge, this work is the first one in signal estimation for vibration of vehicle bodies in the frequency domain. It is believed that using the proposed method with the real test data will facilitate the durability design of vehicle bodies.

The rest of the paper is organized as follows. The problem statement of estimating frequency responses of interesting accelerometers is given in Sec. 2. Then, a nonparametric method for segmentation of the frequency-domain range and a frequency-domain identification method for noncausal FIR models are presented in Secs. 3 and 4, respectively. After that, the performance and the results are shown in Sec. 5. Finally, some concluding remarks are reported in Sec. 6.

2 Scenarios of the Black-Box Identification Problem

In this section, we introduce the black-box identification problem for the vibration of the vehicle body and aims to develop and validate the black-box models from easy-to-measure accelerations to hard-to-measure accelerations.

Figures 1 and 2 show the locations of easy-to-measure and hard-to-measure accelerometers on a sketch of a body frame (top view) and a 3D body frame, respectively, and some accelerometers are also shown in a real test vehicle (Fig. 3). Note that three-axis XYZ accelerometers at the positions marked by "blue bullets" are referred to as easy-to-measure accelerometers (six accelerations in total). The other five accelerometers marked by "red bullets" are hard-to-measure accelerometers, whose frequency signals are aimed to be estimated. There are 14 hard-to-measure accelerations in total, and accelerometer 4 measures only two accelerations in X and Z directions. Both easy-to-measure and hard-to-measure accelerometers are deployed in the test vehicle.

Seventy different working conditions tested in this work can be roughly classified into four categories shown in Table 1, and several road profile examples are shown in Fig. 4. More than 4

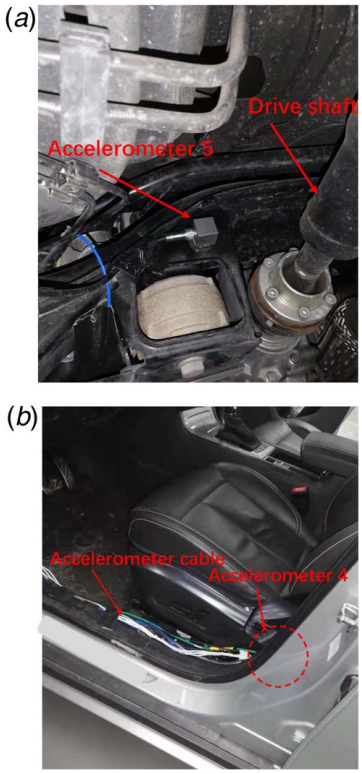

Fig. 3 The locations of two hard-to-measure accelerometers deployed in a test vehicle: (*a*) The hard-to-measure accelerometer 5 is deployed near the drive shaft, (*b*) The hard-to-measure accelerometer 4 is deployed near the driver seat

Table 1 Four categories of working conditions

Category	Description
1.	Driving straight on roads of random or periodic profiles such as Belgium block, smooth gravel, and washboard roads at various vehicle speeds
2.	Driving over bumps, railway crosses, and potholes at various vehicle speeds
3.	Steering at various vehicle speeds
4.	Braking on roads of random or periodic profiles at slight, medium, and heavy levels

$\times 10^4$ data samples are collected for each working condition and the sampling rate is 512 Hz. For working conditions, such as the vehicle being driven over a speed bump or a pothole, we carried out 8–10 experiments because the data length is short in each experiment (approximately 5×10^3 data samples are collected for each experiment). For other working conditions, such as the vehicle is driven at the Belgium block road or smooth gravel road, we carried out only 4–6 experiments because the data length is longer in each experiment (approximately 1×10^4 data samples are collected for each experiment).

The signals collected from accelerometers are time-domain ones, and we transform them into frequency-domain ones for frequency-domain system identification. The frequency resolution of the frequency data is approximately at the range from 0.02 Hz to 0.1 Hz.

Based on the authors' prior knowledge, the possible interesting frequency range is from 0 Hz to 80 Hz and the signals above this range are noises for this specific problem.

The historical data collected under different working conditions are split into two parts: training data and validation data, which will be elaborated in Sec. 5.3. The black-box models describing the relationship between the responses of easy-to-measure accelerations and hard-to-measure accelerations in the frequency domain are constructed using the training data. The constructed models are validated by evaluating the estimation of hard-to-measure accelerations using the validation data. Note that in this work the validation is conducted by a single test vehicle, which is an important and necessary step for the validation by multiple test vehicles.

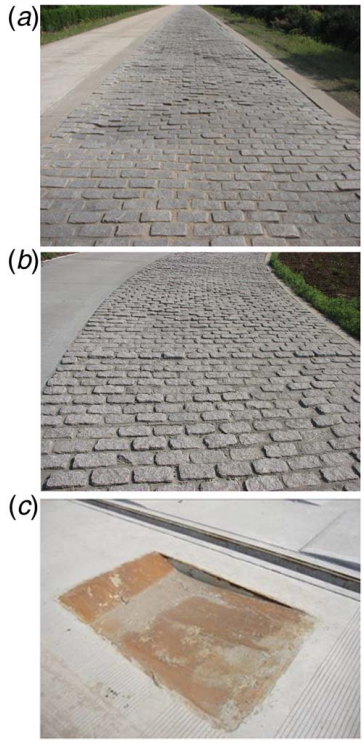

Fig. 4 Three examples of road profiles: (*a*) Belgium block road profile, (*b*) smooth gravel road profile, and (c) pothole road profile

3 Segmentation of the Range in the Frequency Domain

As mentioned in the Introduction, the behavior of the vehicle system could be nonlinear. In this work, we assume that the relation between two subsets of vehicle body accelerations can be approximately represented by piecewise FIR models in the frequency domain. Thus, we propose a nonparametric method to segment the interesting frequency range into several subranges such that FIR models can be constructed over each small subrange. The segmentation is performed in the following three steps:

Determine the noise level in the frequency range from 0 Hz to 80 Hz: The noise may come from two aspects: the measurement noise from accelerometers and the noise from the vehicle itself. Note that the accelerometers in this work are high precision ones and thus the measurement noise of accelerations are assumed to be small enough which can be neglected. Here the noise from the vehicle itself mainly refers to the engine noise which is varying with respect to the vehicle speed. Given an arbitrary frequency response $X(f_{0:80})$, where $f_{0:80}$ denotes the frequency range from 0 Hz to 80 Hz, the noise level is determined as follows. We iteratively go through the following three substeps:

(i) Calculate the mean of the magnitudes of the frequency components in the frequency range from 0 Hz to 80 Hz, where the mean is denoted by $|X(f_{0:80})|_{\text{ave}}$.
(ii) Remove the frequency components whose magnitudes are larger than $\delta|X(f_{0:80})|_{\text{ave}}$ from the current frequency response, where δ is a threshold taken as 3∼5.
(iii) Refresh the frequency response after the removing process above.

The iteration stops until no magnitudes are larger than $\delta|X(f_{0:80})|_{ave}$. Note that $X(f_{0:80})$ is the updated frequency response after the iteration stops. At the end, $|X(f_{0:80})|_{ave}$ is the estimated noise level, and the frequency components whose magnitudes are larger than $\delta|X(f_{0:80})|_{ave}$ are considered as informative frequency signals.

In order to validate the effectiveness of the proposed method for estimating noise levels, we conduct two experiments:

(i) To measure the engine noise, the vehicle is driven on a smooth road at the speed of 50 km h^{-1}.
(ii) The vehicle is driven on a broken cement road at the speed of 50 km h^{-1}.

The effectiveness of the estimation method is validated as follows: we compare the estimated noise level driving on a broken cement road and the measured noise driving on a smooth road. Two examples of the comparison are shown in Fig. 5. We can see that the estimated noise level is close to the measured noise level. Thus, we validate that the proposed estimation method can successfully assess the noise level.

Remark 1. The noise is nonstationary and difficult to estimate. Here we admit that the proposed algorithm is ad hoc. Nevertheless, the approach is effective to some degree in real-world data. Developing an algorithm theoretically to guarantee the estimates of the noise level may become future works.

Select peaks at the frequency range from 0 Hz to 80 Hz: In order to condense the informative frequency signals from the data sets, we select peaks that represent informative signals at the frequency range from 0 Hz to 80 Hz. Note that peaks refer to the frequency signals that are maximum with a neighborhood of 1 Hz. For instance, Fig. 6 shows the interesting peaks at the frequency range from 0 Hz to 80 Hz. Let the threshold be $\delta = 4$. Also, let the frequency components whose magnitudes are larger than $\delta|X(f_{0:80})|_{ave}$ be informative signals. The signals marked by upward-pointing triangles are the selected peaks. Note that the results are

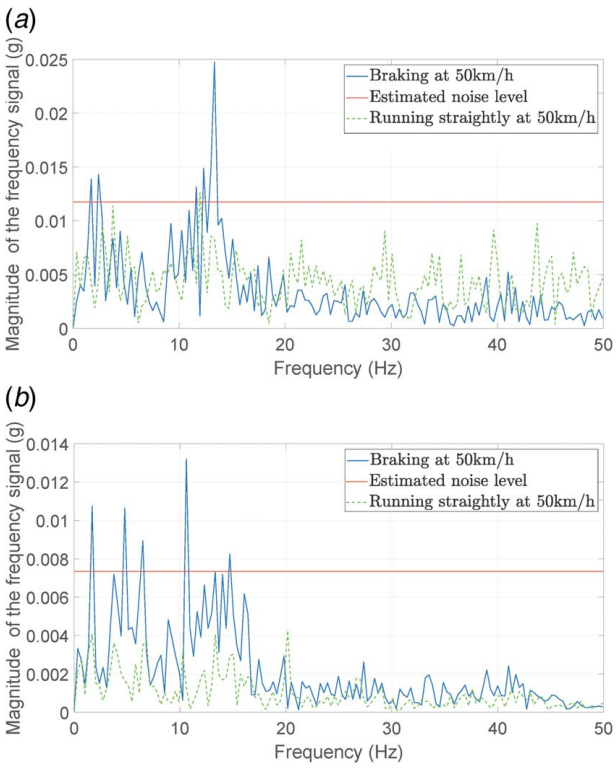

Fig. 5 Two examples of the comparison between the estimated noise level driving on a broken cement road and the measured noise level driving on a smooth road at the same speed: (*a*) the results of accelerometer 1 in *Z* direction, and (*b*) the results of accelerometer 4 in *Z* direction

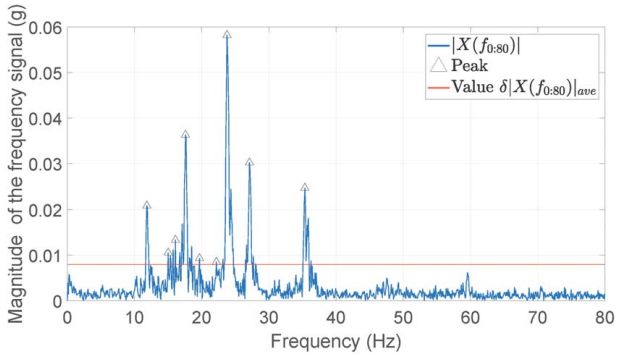

Fig. 6 Illustration of peaks in the frequency domain. Threshold δ is taken as 4.

similar when $\delta = 3$ or 5, and we can conclude that the proposed method can effectively select the main peaks that represent the informative frequency components.

Determine and segment the frequency range from 0 Hz to 80 Hz into subranges: Figure 7 shows the peak histograms of easy-to-measure and hard-to-measure accelerations at the frequency range from 0 Hz to 80 Hz, from which we can draw two conclusions:

(i) From Fig. 7, we can observe that the number of peaks at the frequency range from 50 Hz to 80 Hz is significantly less than the one at the frequency range from 0 Hz to 50 Hz. The reason behind this is that the signal from 50 Hz to 80 Hz contains much noise (almost no peaks in this frequency range), and hence the corresponding signal-to-noise ratio (SNR) in

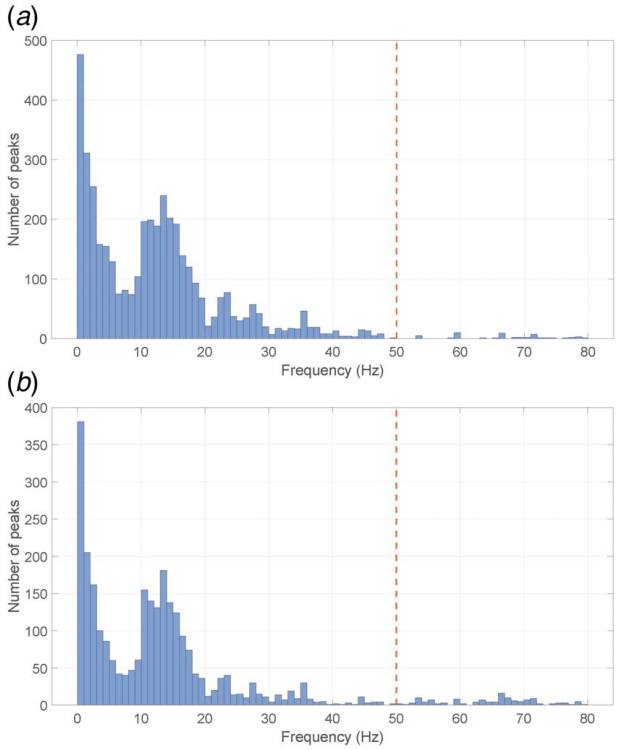

Fig. 7 Peak histograms at the frequency range from 0 Hz to 80 Hz with threshold $\delta = 4$. The data set consists of frequency signals collected under 70 working conditions: (*a*) Peak histogram of six easy-to-measure accelerations at the frequency range from 0 Hz to 80 Hz, (*b*) Peak histogram of 14 hard-to-measure accelerations at the frequency range from 0 Hz to 80 Hz.

this frequency range is much less than that in the frequency range from 0 Hz to 50 Hz. This observation coincides with the engineering experience in the field, where the signals above 50 Hz are less interesting and usually not considered in the vehicle durability design. Thus, we subsequently consider the signal from 0 Hz to 50 Hz.

(ii) We observe that peaks approximately from 4 Hz to 8 Hz and from 18 Hz to 22 Hz are smaller than those of their neighboring frequency ranges. On the other hand, we hope that the splitting subranges used for constructing local FIR models include as many peaks as possible, which indicates that the data are informative. Thus, a reasonable choice is to split the frequency range into ranges from 0 Hz to 6 Hz, 6 Hz to 20 Hz, and 20 Hz to 50 Hz.

Remark 2. We may further segment the frequency range into more subranges. From our experiences on the real-world data, it has no significant improvement on the fitting performance. Also, it may need more training data in the identification of FIR models at each subrange, and the computational cost would increase when the frequency range is segmented into too many subranges.

Furthermore, we choose the working conditions in Table 1 for constructing FIR models in the frequency domain. It is noted that the SNRs of the interesting frequency ranges should be sufficient under the chosen working conditions. The reason behind this is the easy-to-measure variables that are corrupted by the noise (e.g., the engine noise), which could degenerate the identification accuracy of FIR models [25,29]. Thus, we construct the FIR models by choosing the working conditions under which the frequency responses contain as many high peaks as possible, such that the effect of the noise corrupting the easy-to-measure variables can be reduced as much as possible. Figure 8 shows the signals in the frequency domain when the vehicle is driven under several typical working conditions, from which we can see that the working conditions for constructing the FIR models can be determined as follows:

(i) Working condition set $\mathcal{W}_1$: the working conditions under which the driver of the test vehicle is braking or steering are used for constructing the FIR model at the frequency range from 0 Hz to 6 Hz.

(ii) Working condition set $\mathcal{W}_2$: the working conditions under which the test vehicle is driven on roads with random or periodic profiles, such as Belgium block and smooth gravel roads, are used for constructing the FIR model at the frequency range from 6 Hz to 20 Hz.

(iii) Working condition set $\mathcal{W}_3$: the working conditions under which the test vehicle is driven on washboard road are used for constructing the FIR model at the frequency range from 20 Hz to 50 Hz.

Given three subranges and working condition sets above, three different FIR models can be constructed, one for each, aiming at providing a satisfactory description of the relation between the easy-to-measure and hard-to-measure accelerations.

4 Identification of Piecewise Linear Finite Impulse Response Models

In this section, we elaborate on the identification of noncausal FIR models at subranges from 0 Hz to 6 Hz, 6 Hz to 20 Hz, and 20 Hz to 50 Hz. First, we consider a system identification method for identifying multiple-inputs single-output (MISO) FIR models in the frequency domain in Sec. 4.1. Without loss of generality, 14 hard-to-measure accelerations can be estimated independently. Then, two practical considerations regarding to regularization and merging multiple experimental data sets are taken into account in Sec. 4.2. Finally, the piecewise linear FIR models are given in Sec. 4.3.

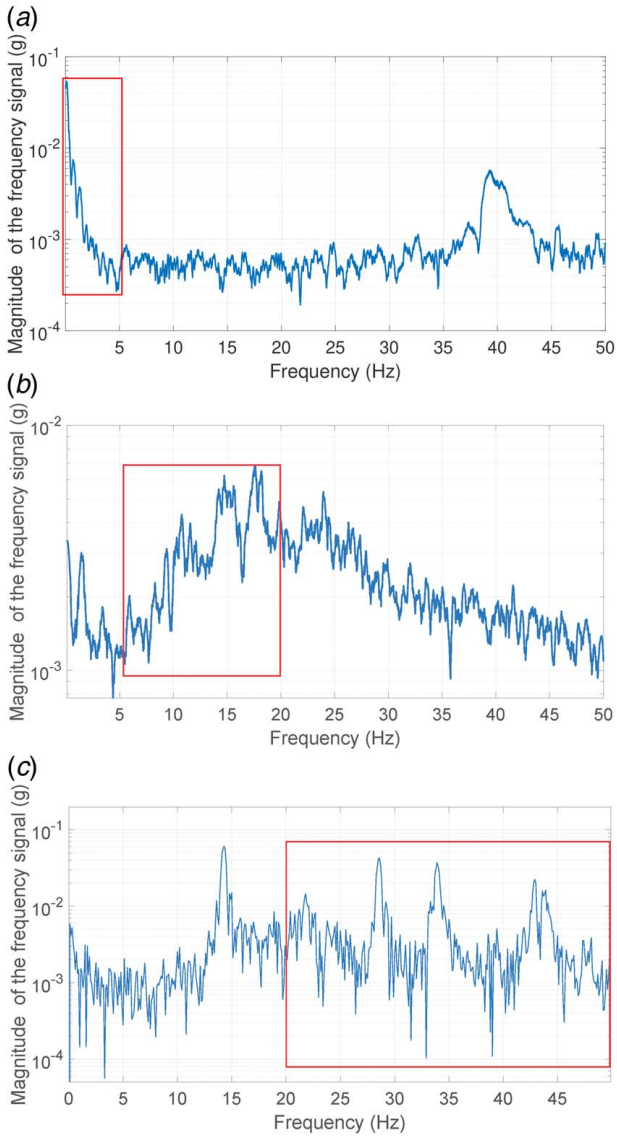

Fig. 8 The signals in the frequency domain when the vehicle is driven under several typical working conditions: (*a*) Signals in the frequency domain when the driver of test vehicle is steering. The SNR is high at the frequency range from 0 Hz to 6 Hz, (*b*) Signals in the frequency domain when the vehicle is driven on the Belgium block road. The SNR is high at the frequency range from 6 Hz to 20 Hz, and (*c*) Signals in the frequency domain when the vehicle is driven on washboard road. The SNR is high at the frequency range from 20 Hz to 50 Hz

4.1 Identification of Noncausal Finite Impulse Response Models. Consider the system diagram of the vehicle vibration system shown in Fig. 9. Let $y_I \in \mathbb{R}^m$ denote easy-to-measure accelerations, an arbitrary hard-to-measure acceleration is denoted by

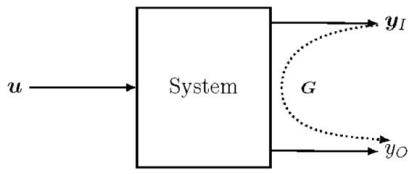

Fig. 9 The system diagram of sensor-to-sensor problems, where $y_I \in \mathbb{R}^m$ is the easy-to-measure signals, $y_O \in \mathbb{R}$ is the hard-to-measure signal, and u is the unknown input

$y_O \in \mathbb{R}$, and u (its dimension is less than or equal to m) denotes the unknown excitation from roads.

Given the specific working condition set (e.g., the working condition set $\mathcal{W}_1$, $\mathcal{W}_2$, or $\mathcal{W}_3$), assume that the system is LTI, and then the relation from y_I to y_O can be described as a transmissibility [21]. Furthermore, the transmissibility can be approximated by a discrete-time noncausal FIR model [25]

$$y_O(t) = G(\mathbf{q})y_I(t) + \epsilon(t) \tag{1}$$

where $\epsilon(t)$ is the residual, $\mathbf{q}$ is the forward shift operator, i.e., $\mathbf{q}\, y_I(t) = y_I(t+1)$, and $G(\mathbf{q}) = \left(G_1(\mathbf{q}) \cdots G_m(\mathbf{q})\right)$ is a row vector. For the sake of simplicity, all $G_j(\mathbf{q})$'s are of the same order and are given by

$$G_j(\mathbf{q}) = \sum_{\ell=-d}^{r} b_{\ell,j}\mathbf{q}^{-\ell}, \quad j = 1, \ldots, m \tag{2}$$

where $b_{-d,j}$,…, $b_{0,j}$,…, $b_{r,j}$ are Markov parameters.

Let $\{y_O(t)\}_0^{N-1}$ be a finite sequence, then the discrete Fourier transform (DFT) of the sequence $\{y_O(t)\}_0^{N-1}$ is defined as

$$Y_O(\omega_k) = \mathrm{DFT}\{\mathrm{y_O(t)}\}_0^{\mathrm{N-1}} = \frac{1}{\mathrm{N}}\sum_{\mathrm{t=0}}^{\mathrm{N-1}} \mathrm{y_O(t)e^{-i\omega_k t}} \tag{3}$$

where $\omega_k = 2\pi k/N$, $k = 0, \ldots, N-1$. Similarly, let $Y_I(\omega_k)$ be the DFT of $y_I(t)$, and $Y_I(\omega_k) = \begin{bmatrix} Y_{I,1}(\omega_k) & \cdots & Y_{I,m}(\omega_k) \end{bmatrix}^T$.

For large data size N, it is a well-known fact [29,33] that the DTFs $Y_I(\omega_k)$ and $Y_O(\omega_k)$ satisfy

$$Y_O(\omega_k) = G(e^{i\omega_k})Y_I(\omega_k) + E(\omega_k) \tag{4}$$

where $E(\omega_k)$ is the residual, and

$$G_j(e^{i\omega_k}) = (R_c(\omega_k) - iI_s(\omega_k))^T b_j, \quad j = 1, \ldots, m \tag{5}$$

where

$$R_c = \begin{bmatrix} \cos(d\omega_k) \\ \vdots \\ 1 \\ \cos(\omega_k) \\ \vdots \\ \cos(r\omega_k) \end{bmatrix}, \quad I_s = \begin{bmatrix} \sin(-d\omega_k) \\ \vdots \\ 0 \\ \sin(\omega_k) \\ \vdots \\ \sin(r\omega_k) \end{bmatrix}, \quad b_j = \begin{bmatrix} b_{-d,j} \\ \vdots \\ b_{0,j} \\ b_{1,j} \\ \vdots \\ b_{r,j} \end{bmatrix} \tag{6}$$

Note that the transient effect is neglected in Eq. (4) when the data size N is large, which is easily guaranteed in this work. Rewriting Eq. (5) yields

$$G(e^{i\omega_k}) = (R_c(\omega_k) - iI_s(\omega_k))^T B \tag{7}$$

where $B = (b_1 \ldots b_m)$ is an $(n+1)\times m$ matrix whose entries are model parameters. Also, $Y_O(\omega_k)$ and $Y_I(\omega_k)$ are expressed as the sum of real and imaginary components

$$\begin{aligned} Y_O(\omega_k) &= R_{Y_O}(\omega_k) + iI_{Y_O}(\omega_k) \\ Y_I(\omega_k) &= R_{Y_I}(\omega_k) + iI_{Y_I}(\omega_k) \end{aligned} \tag{8}$$

where $R_{Y_O}(\omega_k)$ and $I_{Y_O}(\omega_k)$ are real and imaginary components of $Y_O(\omega_k)$, respectively. Similarly, $R_{Y_I}(\omega_k)$ and $I_{Y_I}(\omega_k)$ are real and imaginary components of $Y_I(\omega_k)$, respectively. Substituting Eqs. (7) and (8) into Eq. (4) yields

$$\begin{aligned} &R_{Y_O}(\omega_k) + iI_{Y_O}(\omega_k) \\ &\quad = (R_c(\omega_k) - iI_s(\omega_k))^T B(R_{Y_I}(\omega_k) + iI_{Y_I}(\omega_k)) + E(\omega_k) \end{aligned} \tag{9}$$

By using the property of Kronecker product [34], Eq. (9) can be rewritten as

$$\begin{aligned} &R_{Y_O}(\omega_k) + iI_{Y_O}(\omega_k) \\ &\quad = (R_{Y_I}(\omega_k) + iI_{Y_I}(\omega_k))^T \otimes (R_c(\omega_k) - iI_s(\omega_k))^T\theta + E(\omega_k) \end{aligned} \tag{10}$$

where $\theta = \mathrm{vec}(B)$. By rearranging Eq. (10), we have

$$\begin{bmatrix} R_{Y_O}(\omega_k) \\ I_{Y_O}(\omega_k) \end{bmatrix} = \begin{bmatrix} \phi(\omega_k) & \psi(\omega_k) \end{bmatrix}^T\theta + \begin{bmatrix} R_E(\omega_k) \\ I_E(\omega_k) \end{bmatrix} \tag{11}$$

where

$$\phi(\omega_k) = R_{Y_I}(\omega_k) \otimes R_c(\omega_k) + I_{Y_I}(\omega_k) \otimes I_s(\omega_k) \tag{12}$$

$$\psi(\omega_k) = I_{Y_I}(\omega_k) \otimes R_c(\omega_k) - R_{Y_I}(\omega_k) \otimes I_s(\omega_k) \tag{13}$$

and $R_E(\omega_k)$ and $I_E(\omega_k)$ are real and imaginary parts of the residual $E(\omega_k)$, respectively. Aggregating over all frequencies ω_k at specific subrange (e.g., from 6 Hz to 20 Hz), we have

$$\begin{bmatrix} \Gamma_{R_{Y_O}} \\ \Gamma_{I_{Y_O}} \end{bmatrix} = \begin{bmatrix} \Pi_\phi \\ \Pi_\psi \end{bmatrix}\theta + \begin{bmatrix} \Xi_{R_E} \\ \Xi_{I_E} \end{bmatrix} \tag{14}$$

where

$$\Gamma_{R_{Y_O}} = \begin{bmatrix} R_{Y_O}(\omega_0) \cdots R_{Y_O}(\omega_{N-1}) \end{bmatrix}^T \tag{15}$$

$$\Gamma_{I_{Y_O}} = \begin{bmatrix} I_{Y_O}(\omega_0) \cdots I_{Y_O}(\omega_{N-1}) \end{bmatrix}^T \tag{16}$$

$$\Pi_\phi = \begin{bmatrix} \phi(\omega_0) \cdots \phi(\omega_{N-1}) \end{bmatrix}^T \tag{17}$$

$$\Pi_\psi = \begin{bmatrix} \psi(\omega_0) \cdots \psi(\omega_{N-1}) \end{bmatrix}^T \tag{18}$$

$$\Xi_{R_E} = \begin{bmatrix} R_E(\omega_0) \cdots R_E(\omega_{N-1}) \end{bmatrix}^T \tag{19}$$

$$\Xi_{I_E} = \begin{bmatrix} I_E(\omega_0) \cdots I_E(\omega_{N-1}) \end{bmatrix}^T \tag{20}$$

Equation (14) can be rewritten as

$$\Gamma = \Pi\theta + \Xi \tag{21}$$

where

$$\Gamma = \begin{bmatrix} \Gamma_{R_{Y_O}} \\ \Gamma_{I_{Y_O}} \end{bmatrix}, \quad \Pi = \begin{bmatrix} \Pi_\phi \\ \Pi_\psi \end{bmatrix}, \quad \Xi = \begin{bmatrix} \Xi_{R_E} \\ \Xi_{I_E} \end{bmatrix} \tag{22}$$

The least squares solution of θ is given by

$$\hat{\theta} = (\Pi^T\Pi)^{-1}\Pi^T\Gamma \tag{23}$$

provided that Π is of full column rank.

Remark 3. We decompose complex signals into real and imaginary parts in the derivation of θ such that Eq. (21) produces a real-valued estimate of θ. The fact that the estimate of θ is a real value is not guaranteed in the conventional formulation of FIR system identification methods [29,35], unless two distinct subranges of frequencies are jointly considered, i.e., the subrange $\mathcal{K}_1 = \{\omega_i, \ldots, \omega_f\}$ and the subrange $\mathcal{K}_2 = \{\omega_{N-f}, \ldots, \omega_{N-i}\}$, where N is the size of data set, $i \geq 0$, $f \leq \lfloor \frac{N}{2} \rfloor$, and $\lfloor \cdot \rfloor$ is floor operator. However, the subrange $\mathcal{K}_2$ is essentially unnecessary in our method. The reason is that the complex signals at the subranges $\mathcal{K}_1$ and $\mathcal{K}_2$ are complex conjugate of each other, i.e.,

$$X(\omega_{N-1-k}) = \frac{1}{N}\sum_{t=0}^{N-1} x(t)e^{-i\frac{N-1-k}{N}2\pi t} \tag{24}$$

$$= \frac{1}{N}\sum_{t=0}^{N-1} x(t)e^{-i\frac{-(k+1)}{N}2\pi t} = \bar{X}(\omega_k) \tag{25}$$

where $\omega_k \in \{\omega_i, \ldots, \omega_f\}$, $x(t)$ denotes either $y_I(t)$ or $y_O(t)$ in the time domain, $X(\cdot)$ is the DFT of $x(t)$, and $\bar{X}(\cdot)$ is the complex conjugate of

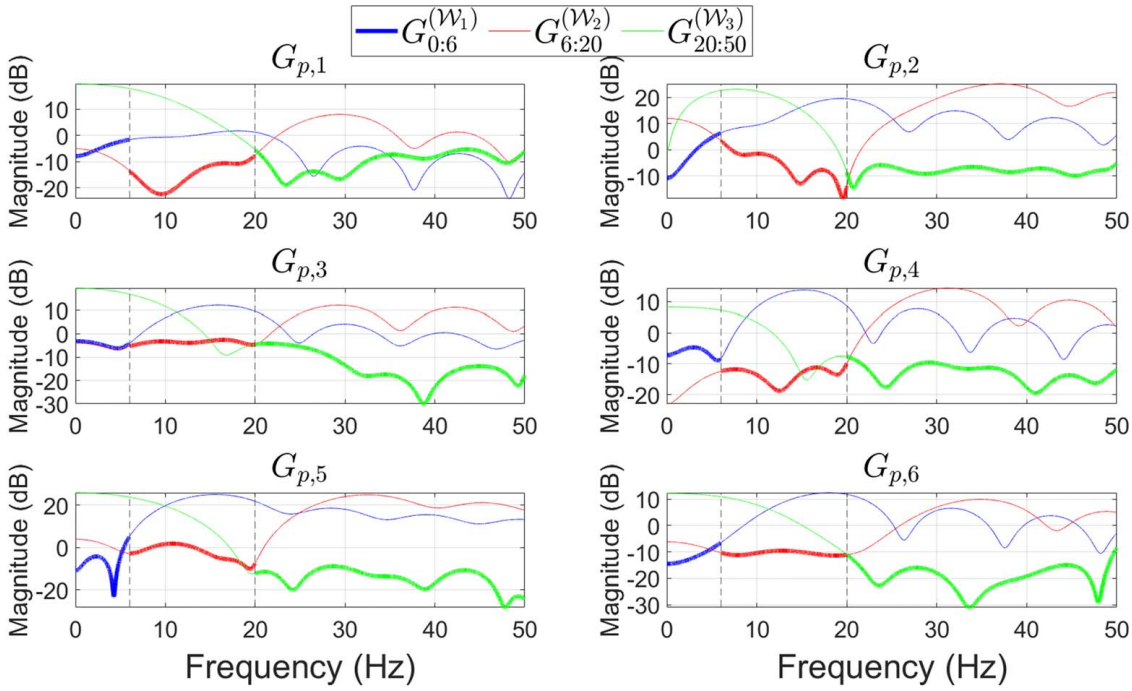

Fig. 10 An example of estimated results of piecewise linear FIR models as FRFs curves. Note that $G_{p,1}, \ldots, G_{p,6}$ are components of the FRFs.

$X(\cdot)$. Also, regarding to Eqs. (12) and (13), it is easily verified that

$$\begin{aligned} \phi(\omega_{N-1-k}) &= \phi(\omega_k) \\ \psi(\omega_{N-1-k}) &= -\psi(\omega_k) \end{aligned} \tag{26}$$

which indicates that redundant information is used when two distinct subranges are considered in Eq. (21). Thus, when constructing Γ and Π in Eq. (21), we only need the information at the frequency subrange $\mathcal{K}_1$.

Remark 4. One of the attractive factors of the FIR model is its BIBO property such that the estimation for hard-to-measure accelerations is stable.

4.2 Practical Considerations. *Regularization*: An issue arises when the matrix Π in Eq. (23) is not full of column rank with two possible reasons:

(i) The model order r and d are unknown and it might be selected too large such that the FIR model is over-fitting [36].
(ii) Multicollinearity among easy-to-measure accelerations (e.g., some of accelerations are redundant) occurs.

Here, a regularization technique is introduced to tackle this issue: The order of an FIR model is typically quite large (a couple of hundred or so [37]), and hence we select a relatively large order (e.g., 100). According to Eq. (21), a regularized least squares (RLS) problem is considered

$$\underset{\theta}{\text{minimize}} \quad \|\Gamma - \Pi\theta\|_2^2 + \lambda\theta^T\theta \tag{27}$$

where $\lambda\theta^T\theta$ is a flexibility term, and λ is a tuning parameter [36]. The optimization problem (27) admits a closed-form solution

$$\hat{\theta}^{\text{ridge}} = (\Pi^T\Pi + \lambda\mathbf{I})^{-1}\Pi^T\Gamma \tag{28}$$

where $\mathbf{I}$ is an identity matrix with the compatible dimension. In this case, the form of the RLS problem (27) is called *ridge regression*, and we can use a common general tool called *cross validation* to choose an appropriate value of λ [36].

Merging multiple experiments: When multiple experiments for constructing FIR models are conducted under different working conditions, under which the data size and the input power levels are varied, the RLS problem (27) can be revised as

$$\underset{\theta}{\text{minimize}} \quad \sum_{h=1}^{H} \frac{1}{\|\Gamma_h\|_2^2}\{\|\Gamma_h - \Pi_h\theta\|_2^2\} + \lambda\theta^T\theta \tag{29}$$

where Γ_h and Π_h are corresponding matrices in Eq. (27) in the hth experiment, and H is the number of experiments. The solution to the problem (29) is

$$\hat{\theta} = \left[\sum_{h=1}^{H} \frac{\Pi_h^T\Pi_h}{\|\Gamma_h\|_2^2} + \lambda\mathbf{I}\right]^{-1}\left[\sum_{h=1}^{H} \frac{1}{\|\Gamma_h\|_2^2}\Pi_h^T\Gamma_h\right] \tag{30}$$

Remark 5. Given the situations that the signal magnitudes and data sizes from various experiments are different, the values $1/\|\Gamma_h\|$'s serve as weighting parameters to "equally" value the importance of H experiments.

4.3 Piecewise Linear Finite Impulse Response Models in the Frequency Domain. According to the identification of FIR models in the subranges from 0 Hz to 6 Hz, 6 Hz to 20 Hz, and 20 Hz to 50 Hz introduced in Sec. 4.1 and Sec. 4.2, the piecewise linear FIR model can be represented as follows:

$$G_p\left(e^{\frac{i2\pi f_k}{F_s}}\right) = \begin{cases} G_{0:6}^{(\mathcal{W}_1)}\left(e^{\frac{i2\pi f_k}{F_s}}\right), & 0 \le f_k < 6 \\ G_{6:20}^{(\mathcal{W}_2)}\left(e^{\frac{i2\pi f_k}{F_s}}\right), & 6 \le f_k < 20 \\ G_{20:50}^{(\mathcal{W}_3)}\left(e^{\frac{i2\pi f_k}{F_s}}\right), & 20 \le f_k \le 50 \end{cases} \tag{31}$$

where $G_p(e^{i2\pi f_k/F_s})$ is the piecewise linear FIR model, $f_k = (k/N)F_s$, $k = 0, \ldots, N-1$, F_s is the sampling frequency, $G_{0:6}^{(\mathcal{W}_1)}$ is the trained FIR model constructed from the data of working condition set $\mathcal{W}_1$ in the frequency subrange from 0 Hz to 6 Hz. Similarly, $G_{6:20}^{(\mathcal{W}_2)}$ is the trained FIR model constructed from the data of working condition set $\mathcal{W}_2$ in the frequency subrange from 6 Hz to 20 Hz, and $G_{20:50}^{(\mathcal{W}_3)}$ is the trained FIR model constructed from the data of working condition set $\mathcal{W}_3$ in the frequency subrange from 20 Hz to 50 Hz.

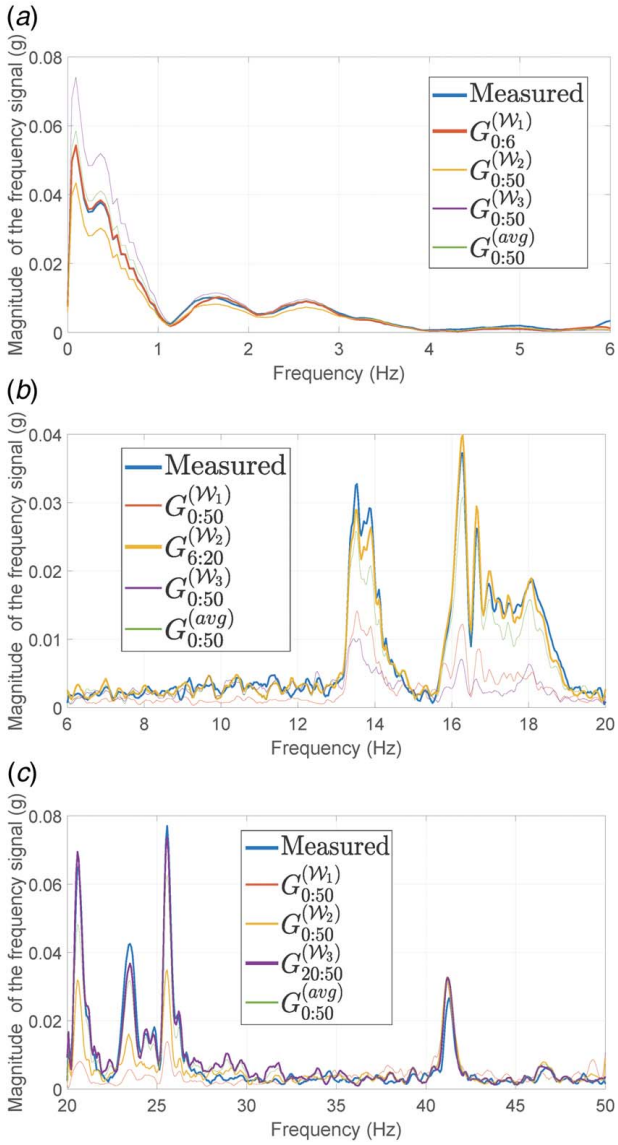

Fig. 11 The examples of estimated results of piecewise linear estimator and individual FIR estimators: (*a*) the results of accelerometer 4 in *Z* direction, (*b*) the results of accelerometer 4 in *Z* direction, and (c) the results of accelerometer 4 in *Z* direction

Figure 10 shows the frequency response function (FRF) curves from 0 Hz to 50 Hz, from which we can observe that the FRFs are significantly different in different subranges, which indicates that the system is nonlinear.

5 Results and Performance

In this section, we investigate the performance of the piecewise linear system identification method proposed in Secs. 3 and 4. First, a comparative study between the piecewise linear FIR models and the individual FIR linear models is conducted in Sec. 5.1. Then, another comparative study between the piecewise linear FIR models and nonlinear models is given in Sec. 5.2. Finally, the overall estimated results of 14 hard-to-measure accelerations under 70 working conditions are discussed in Sec. 5.3.

5.1 A Comparative Study Between the Piecewise Linear Finite Impulse Response Models and the Individual Finite Impulse ResponseModels. In this subsection, we show a comparative study between the piecewise linear estimator G_p shown in

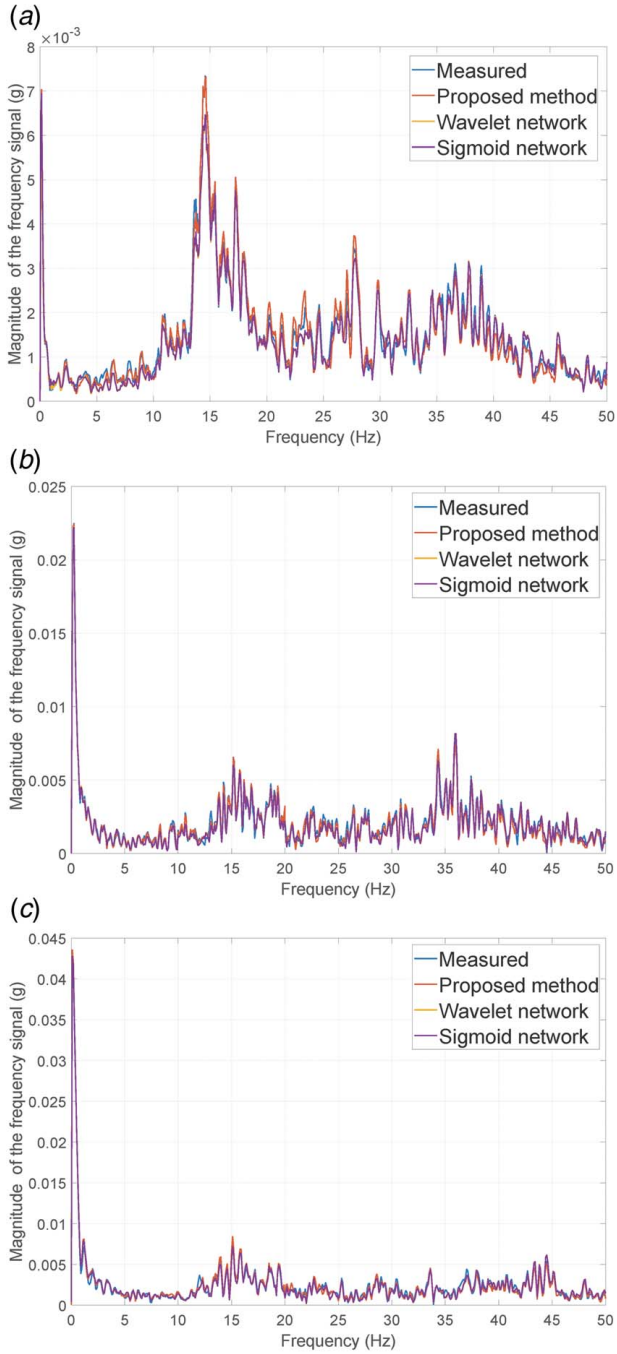

Fig. 12 The estimated results when the vehicle is driven on a smooth gravel road at different vehicle speeds: (*a*) The vehicle is driven at speed of 30 km h^{-1}, (*b*) The vehicle is driven at speed of 40 km h^{-1}, (*c*) The vehicle is driven at speed of 50 km h^{-1}

Sec. 4.3 and four individual linear FIR estimators. Note that we use the data of three working condition sets $\mathcal{W}_1$, $\mathcal{W}_2$, and $\mathcal{W}_3$ from 0 Hz to 50 Hz to construct three individual FIR estimators $G_{0:50}^{(\mathcal{W}_1)}$, $G_{0:50}^{(\mathcal{W}_2)}$, and $G_{0:50}^{(\mathcal{W}_3)}$, respectively. In addition, we use the data of all three working condition sets from 0 Hz to 50 Hz as a whole to construct an "average" FIR estimator denoted by $G_{0:50}^{(avg)}$. Figure 11 shows the estimated examples of individual FIR estimators and the piecewise linear estimators in three subranges, from which we can observe that the piecewise linear FIR estimator outperforms the individual linear estimators in the interesting frequency ranges, which validates the advantage of the piecewise linear estimator.

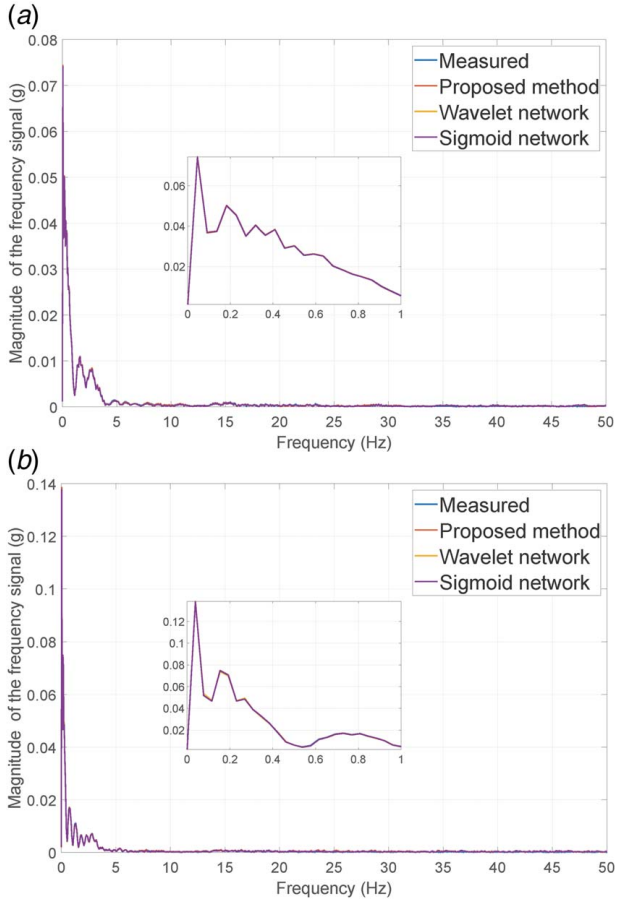

Fig. 13 The estimated results when the driver is braking at different vehicle speeds: (*a*) The driver is braking at speed of 30 km h^{-1}, (*b*) The driver is braking at speed of 70 km h^{-1}

5.2 A Comparative Study of the Piecewise Linear Finite Impulse Response Models and Nonlinear Models. Now the comparative study between the proposed piecewise linear method and the nonlinear system identification methods is conducted under multiple working conditions. Nonlinear system identification methods are often used to build black-box models for complex dynamic systems [38]. In this subsection, two common nonlinear models, wavelet and sigmoid network models [39], are used to estimate the hard-to-measure accelerations under multiple working conditions.

Figures 12–14 show some typical examples of the estimated results of

(i) *steady-state data*: the vehicle is driven on a smooth gravel road at the speeds of 30 km h^{-1}, 40 km h^{-1}, and 50 km h^{-1}, see Fig. 12;
(ii) *transitional data*: the driver is braking at the speeds of 30 km h^{-1} and 70 km h^{-1}, see Fig. 13. Also, the driver is driving across a speed bump at speeds of 10 km h^{-1}, 20 km h^{-1}, and 30 km h^{-1}, see Fig. 14.

Note that these working conditions are not included in the training data sets. From Figs. 12–14, it can be observed that the estimated result from the proposed method and that from the measurements are close to each other, which indicates that the proposed piecewise linear estimator is applicable to the scenarios with different speeds and road profiles. Also, the performance of the proposed piecewise linear method is comparable to that of the nonlinear methods. For better performance of nonlinear methods, more sophisticated nonlinear methods or hyper-parameter tuning methods should be involved, which is difficult to generalize in practice. For example, the modeling process might need to be conducted from the scratch when a new type of prototypes is aimed to be developed.

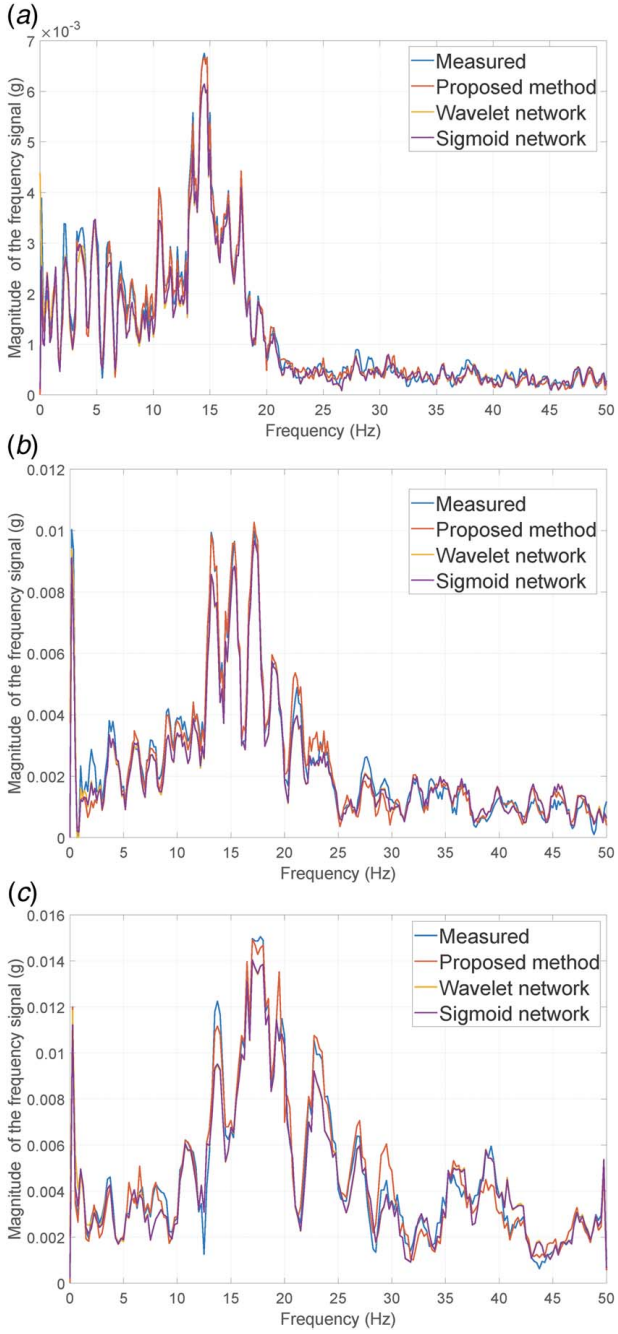

Fig. 14 The estimated results when the vehicle is driven across the speed bump at different speeds: (*a*) The vehicle is driven at speed of 10 km h^{-1}, (*b*) The vehicle is driven at speed of 20 km h^{-1}, (*c*) The vehicle is driven at speed of 30 km h^{-1}

Now we report the run-time of the proposed method and the nonlinear system identification methods. The experiments are conducted using 2.50 Hz Intel Core i5-7200U processor, and all implementations are done in Matlab 2018b. Table 2 shows the run-time of the investigated methods, from which we can see that:

(i) The run-time of the proposed method during the validation stage is much shorter than the actual time duration for the validation (10 s).

Table 2 Run-time of the proposed method and the nonlinear methods

Method	Training	Validation
Proposed method	8.23 s	0.73 s
Wavelet network	236.72 s	1.13 s
Sigmoid network	Over 10 min	5.37 s

Note: The data length in the validation is 10 s.

(ii) The nonlinear methods are much more time-consuming than the proposed one, during both the training and validation stages.

This result indicates that the proposed method is more computationally efficient for real-time estimation.

5.3 Estimated Results of 14 Accelerations Under 70 Working Conditions. Furthermore, we collect the data from 70 working conditions, and 14 hard-to-measure accelerations are required to be estimated.

Given the specific frequency range and a working condition set $\mathcal{W}_\ell$, $\ell = 1, 2, 3$ (cf. Sec. 3), we use a subset of data sets under the working condition set $\mathcal{W}_\ell$ to train the models. The validation consists of self-validation and cross-validation:

(i) In self-validation, the data sets used for validating the effectiveness of the trained models are the remaining data sets under the same working condition set $\mathcal{W}_\ell$.
(ii) In cross-validation, the data sets used for validating the effectiveness of the trained models are from working conditions which are different from the working condition set $\mathcal{W}_\ell$.

In order to evaluate the results quantitatively, we define the normalized mean square error (NMSE) [40–42] as

$$\text{NMSE} = \frac{\|Z - \hat{Z}\|_2^2}{\|Z\|_2^2} \tag{32}$$

where Z is the magnitude vector of frequency signals collected from hard-to-measure accelerometers at specific frequency ranges, and $\hat{Z}$ is the corresponding estimate. Also, we define NMSE = 0.3 as an acceptable level. Note that the value of the acceptable level is recommended by the engineers from SAIC motor company who are responsible for the durability design. Four examples of measured signals and their estimates are shown in Fig. 15.

Figure 16 reports the results of 14 accelerations at three frequency subranges in detail. We divide 980 cases into seven categories, and the total acceptable results (adding up results of category 1, 5, 7) at the three subranges are shown in Table 3, from which we can observe that the acceptable percentages from 0 Hz to 20 Hz are high (around 90%). We also notice that the acceptable percentage in the frequency range from 20 Hz to 50 Hz (around 80%) is lower than that from 0 Hz to 20 Hz. Particularly, the result of category 1 at the frequency range from 20 Hz to 50 Hz is only 20.8%. That is because the SNR of easy-to-measure accelerations at this frequency subrange is lower than those in the other subranges. As shown in Fig. 7, the number of peaks from 20 Hz to 50 Hz is significantly smaller than the number of peaks from other subranges.

Note that the estimated results of both category 5 and 7 are acceptable, because

(i) For the results of category 5, where easy-to-measure signals are informative, hard-to-measure signals and their estimates are noninformative, we validate that both the hard-to-measure signals and their estimates are noninformative, which indicates that the estimator does not make any "mistakes" even though the NMSEs of estimated results might be greater than a threshold.
(ii) For the results of category 7, where both easy-to-measure and hard-to-measure signals are noninformative, there is no

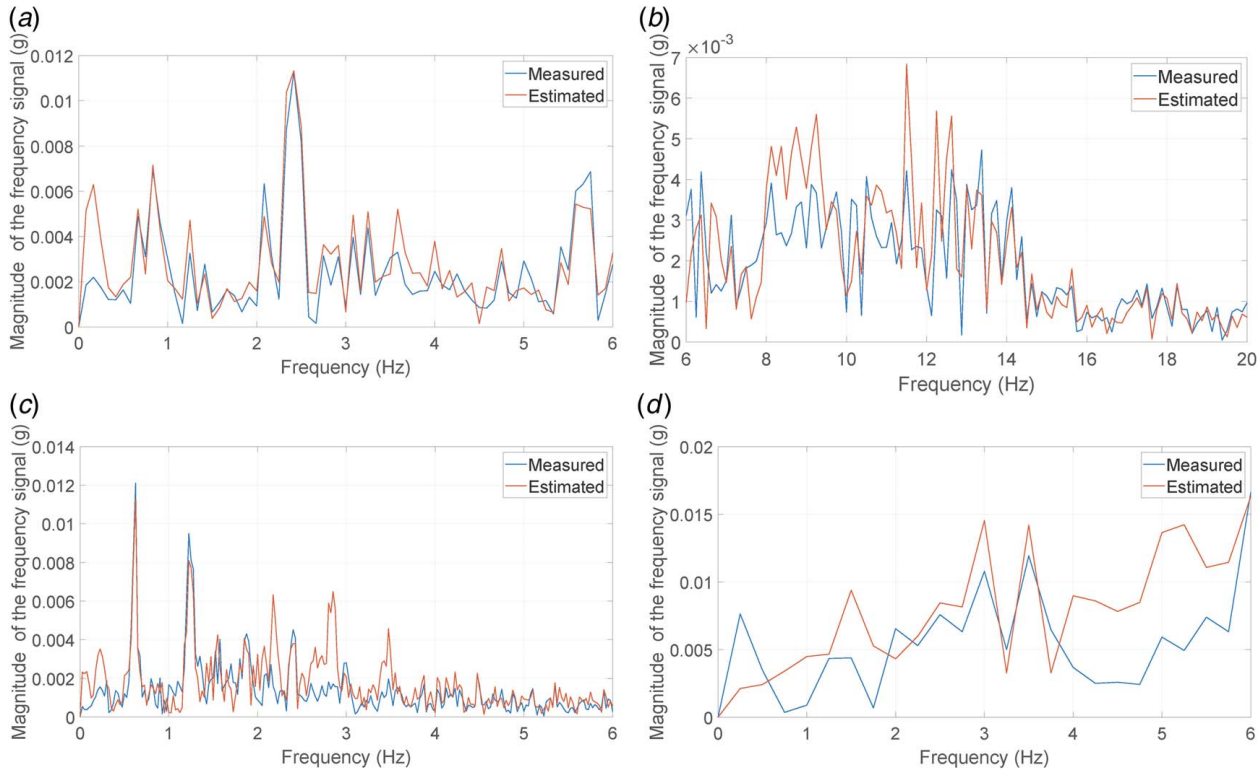

Fig. 15 Four examples of NMSEs. The acceptable level is chosen as NMSE = 0.3: (*a*) Example: NMSE = 0.1, (*b*) Example: NMSE = 0.2, (*c*) Example: NMSE = 0.3, (*d*) Example: NMSE = 0.4.

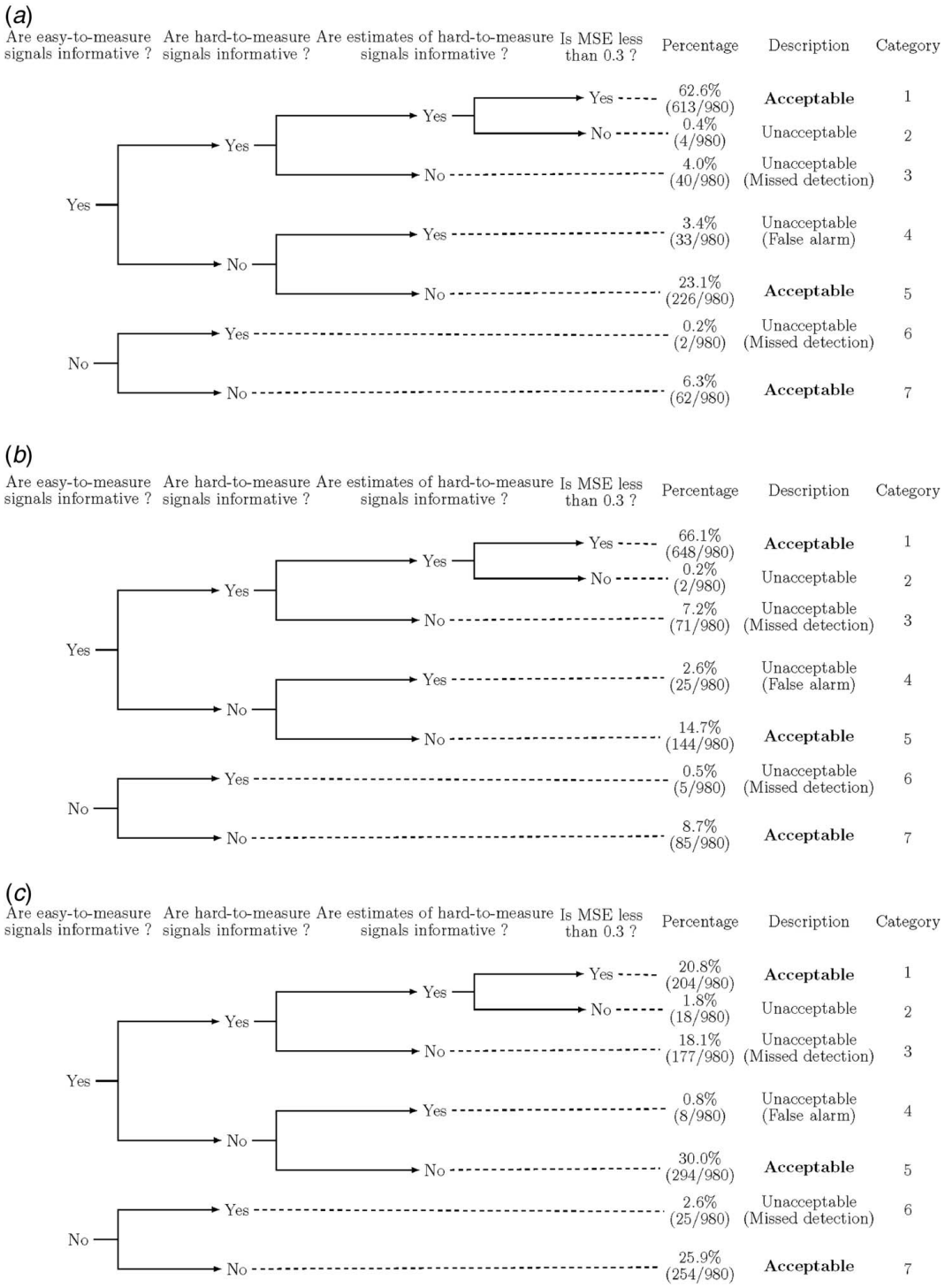

Fig. 16 The estimation result of 14 accelerations at three frequency ranges under 70 working conditions. The procedure of classifying 980 cases is as follows: are easy-to-measure signals informative ? → are hard-to-measure signals informative ? → are estimated hard-to-measure informative ? → Is NMSE less than 0.3 ?: (*a*) The estimation result of 14 accelerations at the frequency range from 0 Hz to 6 Hz under 70 working conditions, (*b*) The estimation result of 14 accelerations at the frequency range from 6 Hz to 20 Hz under 70 working conditions, (c) The estimation result of 14 accelerations at the frequency range from 20 Hz to 50 Hz under 70 working conditions

Table 3 Overall results at three frequency subranges

Frequency range (Hz)	Percentage of acceptable results
0–6	91.9% (901/980)
6–20	90.0% (882/980)
20–50	79.3% (777/980)

need to estimate and we can isolate the data of category 7. Also, the hard-to-measure signals are noninformative, which indicates that the results of category 7 are acceptable.

6 Conclusion

In this work, we present a piecewise linear system identification method in the frequency domain to claim that it is promising to

estimate the responses of hard-to-measure accelerations by the responses of easy-to-measure accelerations. The possible reason behind the success of the piecewise linear system identification method is that the nonlinear dynamic responses are mainly influenced by the frequency of the excitation from roads, as investigated in Ref. [9], and the behaviors of the system are linear in certain frequency ranges.

We verify that FIR models can serve as good candidates for signal estimation in the vehicle body system: by using only two easy-to-measure X, Y, Z accelerometers as the inputs of FIR models, almost 90% estimation accuracy is achieved for 14 hard-to-measure accelerations under 70 working conditions.

Acknowledgment

The work presented here is supported in part by VMAP program of VMware. Such support does not constitute an endorsement by the funding agency of the opinions expressed in the article. We would like to thank Mr. Gavin Lu and Mr. Yixing Jia from VMware Ltd., China, for their kind technical support.

Conflict of Interest

There are no conflicts of interest.

Data Availability Statement

Data provided by a third party listed in Acknowledgment.

References

[1] Risaliti, E., Tamarozzi, T., Vermaut, M., Cornelis, B., and Desmet, W., 2019, "Multibody Model Based Estimation of Multiple Loads and Strain Field on a Vehicle Suspension System," Mech. Syst. Signal Process., **123**, pp. 1–25.
[2] El-kafafy, M., Csurcsia, P., Cornelis, B., Enrico, R., and Janssens, K., 2020, "Machine Learning and System Identification for the Estimation of Data-Driven Models: An Experimental Case Study Illustrated on a Tire-Suspension System," Proceedings of the International Conference on Noise and Vibration Engineering (ISMA), Leuven, Belgium, October, KU Leuven, pp. 3287–3301.
[3] Chung, H., North, C., and Ferris, J., 2013, "Developing Large High-Resolution Display Visualizations of High-Fidelity Terrain Data," ASME J. Comput. Inf. Sci. Eng., **13**(3), p. 034502.
[4] Jiang, Y., Yun, G. J., Zhao, L., and Tao, J., 2015, "Experimental Design and Validation of an Accelerated Random Vibration Fatigue Testing Methodology," Shock Vib., **2015**, p. 147871.
[5] Kadlec, P., Gabrys, B., and Strandt, S., 2009, "Data-Driven Soft Sensors in the Process Industry," Comput. Chem. Eng., **33**(4), pp. 795–814.
[6] Kaneko, H., and Funatsu, K., 2012, "Estimation of Predictive Accuracy of Soft Sensor Models Based on One-Class Support Vector Machine," *Computer Aided Chemical Engineering*, I. A. Karimi and R. Srinivasan, eds., Vol. 31, Elsevier, Amsterdam, The Netherlands, pp. 1246–1250.
[7] Wang, D., Gong, J., Kang, Q., Fan, D., and Yang, J., 2019, "Soft Sensing for Gas-Condensate Field Production Using Parallel-Genetic-Algorithm-Based Data Reconciliation," ASME J. Comput. Inf. Sci. Eng., **19**(4), p. 044501.
[8] Jennings, M., and Rangan, R., 2004, "Managing Complex Vehicle System Simulation Models for Automotive System Development," ASME J. Comput. Inf. Sci. Eng., **4**(4), pp. 372–378.
[9] Zhou, S., Song, G., Sun, M., and Ren, Z., 2016, "Nonlinear Dynamic Analysis of a Quarter Vehicle System With External Periodic Excitation," Int. J. Non-Linear Mech., **84**, pp. 82–93.
[10] Zhu, Q., and Ishitobi, M., 2006, "Chaotic Vibration of a Nonlinear Full-Vehicle Model," Int. J. Solids Struct., **43**(3–4), pp. 747–759.
[11] Wang, G., and Yin, S., 2014, "Data-Driven Fault Diagnosis for an Automobile Suspension System by Using a Clustering Based Method," J. Franklin Inst., **351**(6), pp. 3231–3244.
[12] Dao, T.-K., and Chen, C.-K., 2011, "Path Tracking Control of a Motorcycle Based on System Identification," IEEE Trans. Veh. Technol., **60**(7), pp. 2927–2935.
[13] Michopoulos, J. G., Iliopoulos, A. P., Steuben, J. C., and DeGiorgi, V., 2018, "On the Multiphysics Modeling of Surface Aging Under Cathodic Protection," ASME J. Comput. Inf. Sci. Eng., **18**(3), p. 031001.
[14] Guo, J., He, H., and Sun, C., 2019, "Arima-Based Road Gradient and Vehicle Velocity Prediction for Hybrid Electric Vehicle Energy Management," IEEE Trans. Veh. Technol., **68**(6), pp. 5309–5320.
[15] Moges, T., Yang, Z., Jones, K., Feng, S., Witherell, P., and Lu, Y., 2021, "Hybrid Modeling Approach for Melt-Pool Prediction in Laser Powder Bed Fusion Additive Manufacturing," ASME J. Comput. Inf. Sci. Eng., **21**(5), p. 050902.
[16] Sliwa, B., and Wietfeld, C., 2019, "Towards Data-Driven Simulation of End-to-End Network Performance Indicators," 2019 IEEE 90th Vehicular Technology Conference (VTC2019-Fall), Honolulu, HI, Sept. 22–25, pp. 1–7.
[17] Irshad, L., Demirel, H. O., and Tumer, I. Y., 2020, "Automated Generation of Fault Scenarios to Assess Potential Human Errors and Functional Failures in Early Design Stages," ASME J. Comput. Inf. Sci. Eng., **20**(5), p. 051009.
[18] Wang, Y.-Y., Sun, Y., Chang, C.-F., and Hu, Y., 2016, "Model-Based Fault Detection and Fault-Tolerant Control of SCR Urea Injection Systems," IEEE Trans. Veh. Technol., **65**(6), pp. 4645–4654.
[19] Tosyali, A., Song, R., Guo, W., Abolhassani, A., and Kalamdani, R., 2021, "Data-Driven Gantry Health Monitoring and Process Status Identification Based on Texture Extraction," ASME J. Comput. Inf. Sci. Eng., **21**(1), p. 011003.
[20] Linder, J., and Enqvist, M., 2017, "Identification of Systems With Unknown Inputs Using Indirect Input Measurements," Int. J. Control, **90**(4), pp. 729–745.
[21] Aljanaideh, K. F., and Bernstein, D. S., 2015, "Time-Domain Analysis of Sensor-to-Sensor Transmissibility Operators," Automatica, **53**, pp. 312–319.
[22] Yan, W.-J., Zhao, M.-Y., Sun, Q., and Ren, W.-X., 2019, "Transmissibility-Based System Identification for Structural Health Monitoring: Fundamentals, Approaches, and Applications," Mech. Syst. Signal Process., **117**, pp. 453–482.
[23] Aljanaideh, K. F., and Bernstein, D. S., 2017, "A Behavioral Equation Framework for Time-Domain Transmissibilities," Automatica, **78**, pp. 20–24.
[24] Khalil, A., and Aljanaideh, K. F., 2018, "Aircraft Structural Health Monitoring Using Transmissibility Identification," IFAC-PapersOnLine, **51**(15), pp. 969–974.
[25] Aljanaideh, K. F., and Bernstein, D. S., 2020, "Output-Only Identification of Input–Output Models," Automatica, **113**, p. 108686.
[26] Gao, F., and Nallanathan, A., 2008, "Resolving Multidimensional Ambiguity in Blind Channel Estimation of MIMO-FIR Systems Via Block Precoding," IEEE Trans. Veh. Technol., **57**(1), pp. 11–21.
[27] Liu, J., 2009, "Be Cautious When Using the FIR Channel Model With the OFDM-Based Communication Systems," IEEE Trans. Veh. Technol., **58**(3), pp. 1607–1612.
[28] de Lamare, R. C., and Sampaio-Neto, R., 2007, "Adaptive Interference Suppression for DS-CDMA Systems Based on Interpolated FIR Filters With Adaptive Interpolators in Multipath Channels," IEEE Trans. Veh. Technol., **56**(5), pp. 2457–2474.
[29] Soverini, U., and Söderström, T., 2020, "Frequency Domain Identification of FIR Models in the Presence of Additive Input–Output Noise," Automatica, **115**, p. 108879.
[30] Colin, K., Bombois, X., Bako, L., and Morelli, F., 2019, "Informativity: How to Get Just Sufficiently Rich for the Identification of MISO FIR Systems With Multisine Excitation," 2019 18th European Control Conference (ECC), Naples, Italy, August, pp. 351–356.
[31] Kukreja, S. L., and Bernstein, D. S., 2012, Sensor-Only System Identification for Structural Health Monitoring of Advanced Aircraft, Technical Report, NASA Armstrong Flight Research Center.
[32] Lennart, L., 1999, *System Identification: Theory for the User*, PTR Prentice Hall, Upper Saddle River, NJ, pp. 1–14.
[33] Pintelon, R., and Schoukens, J., 2012, *System Identification: A Frequency Domain Approach*, IEEE, New York
[34] Magnus, J. R., and Neudecker, H., 2019, *Matrix Differential Calculus With Applications in Statistics and Econometrics*, Wiley, Hoboken, NJ.
[35] Kueiming, L., Wook, H.K., 2002, "A New Identification Approach for FIR Models," IEEE Trans. Circuits Syst. II: Analog Digital Signal Process, **49**(6), pp. 439–446.
[36] Ljung, L., and Chen, T., 2013, "What Can Regularization Offer for Estimation of Dynamical Systems?," 11th IFAC International Workshop on Adaptation and Learning in Control and Signal Processing (ALCOSP13), July 3–5, Caen, France, IFAC, pp. 1–8.
[37] Chen, T., and Ljung, L., 2013, "Implementation of Algorithms for Tuning Parameters in Regularized Least Squares Problems in System Identification," Automatica, **49**(7), pp. 2213–2220.
[38] Kerschen, G., Worden, K., Vakakis, A. F., and Golinval, J.-C., 2006, "Past, Present and Future of Nonlinear System Identification in Structural Dynamics," Mech. Syst. Signal Process., **20**(3), pp. 505–592.
[39] Ljung, L., 1995, *System Identification Toolbox: User's Guide*, Citeseer.
[40] Raghavendra, M., and Giridhar, K., 2004, "Improving Channel Estimation in OFDM Systems for Sparse Multipath Channels," IEEE Signal Process. Lett., **12**(1), pp. 52–55.
[41] Raghavendra, M., Bhashyam, S., and Giridhar, K., 2005, "Exploiting Hopping Pilots for Parametric Channel Estimation in OFDM Systems," IEEE Signal Process. Lett., **12**(11), pp. 737–740.
[42] Xie, H., Andrieux, G., Wang, Y., Diouris, J.-F., and Feng, S., 2014, "Efficient Time Domain Threshold for Sparse Channel Estimation in OFDM System," AEU-Int. J. Electron. Commun., **68**(4), pp. 277–281.